

Anomalous Nernst Effect in Dirac Semimetal Cd_3As_2

Tian Liang^{1*}, Jingjing Lin^{1*}, Quinn Gibson², Tong Gao¹, Max Hirschberger¹, Minhao Liu¹, R. J. Cava², and N. P. Ong¹

Departments of Physics¹ and Chemistry², Princeton University, Princeton, NJ 08544

(Dated: October 11, 2016)

Dirac and Weyl semimetals have attracted strong interests. In Cd_3As_2 , the Dirac nodes split into Weyl states under magnetic field, which leads to a remarkable protection mechanism that strongly suppresses backscattering in zero magnetic field, resulting in ultrahigh mobility ($\sim 10^7 \text{ cm}^2 \text{ V}^{-1} \text{ s}^{-1}$). Anomalous Nernst effect is predicted to occur due to the Berry curvature coming from the Weyl nodes. Seebeck and Nernst measurements were performed on Cd_3As_2 and large anomalous Nernst effect was observed. The magnitude of anomalous Nernst signals develops rapidly below $\sim 50 \text{ K}$ where the transport relaxation time τ_{tr} starts to evolve, suggesting close relation between the protection mechanism and the anomalous Nernst effect. Under magnetic field, quantum oscillations show beating effect, suggesting the Dirac nodes split into Weyl states.

PACS numbers:

Topological materials have been one of the central topics in condensed matter physics. Recently Dirac and Weyl semimetals have attracted considerable attention [1]. Dirac and Weyl semimetals are the 3D analogue of graphene. In Dirac semimetals, by either breaking the time reversal or inversion symmetry, the Dirac nodes split into Weyl states. The Weyl states consist of monopoles and antimonopoles in momentum space [2, 3] which play as the sources and sinks of the Berry curvature. Since each 2D plane perpendicular to the line connecting the Weyl nodes can be regarded as the 2D Chern insulator, Fermi arcs appear as the set of the chiral edge states of each plane, which was observed by photoemission experiments [4]. In Dirac semimetals Cd_3As_2 [5] and Na_3Bi [6], C_4 and C_3 rotational symmetry protect the Weyl nodes from merging with each other, preventing the system from opening a gap at zero magnetic field, where two Weyl nodes sit with each other at the same point in momentum space.

One of the interesting phenomena in Dirac and Weyl semimetals related to the Berry curvature is the chiral anomaly, i.e., the breaking of chiral charge conservation between the left handed and right handed electrons. This was derived both in the ultra-quantum limit [7] and in the semiclassical limit at low fields [8]. Experimentally, the chiral anomaly appears as negative longitudinal magnetoresistance (LMR) that locks along the direction of $\mathbf{E} \parallel \mathbf{B}$ as the sharp conductivity plume, which was observed in Na_3Bi [9] and GdPtBi [10]. Negative LMR is also reported in other systems such as $\text{Bi}_{1-x}\text{Sb}_x$ [11], Cd_3As_2 [12, 13], ZrTe_5 [14], TaAs [15] etc.

The effects of Berry curvature coming from the monopoles and antimonopoles of Weyl nodes, however, are not restricted to chiral anomaly. Anomalous Hall effect (AHE) or equivalently anomalous Nernst effect (ANE) is expected to occur [16], with the anomalous Hall conductivity expressed as [1],

$$\sigma_{\text{AHE}} = \frac{e^2}{2\pi h} \left| \sum \Delta \mathbf{k}_i \right| \quad (1)$$

where $\Delta \mathbf{k}_i$ is the distance between the i^{th} pair of Weyl nodes. Indeed, recent calculation [17] implies that ANE occurs in Dirac semimetals under magnetic field or time reversal broken Weyl semimetals.

In current experiments, thermoelectric responses are investigated for two set A samples A4, A5 and two set B samples B10, B20 (see Ref. [12] for details of the electrical transport measurements for set A and set B samples), with a thermal gradient $-\nabla T \parallel \hat{\mathbf{x}}$ and applied magnetic field $\mathbf{B} \parallel \hat{\mathbf{z}}$. The diffusion of carriers produces an electric field \mathbf{E} which is expressed as the thermopower signal $S_{xx} = -E_x/|\nabla T|$, and the Nernst signal $S_{xy} = E_y/|\nabla T|$. In an infinite medium, the total current density is given by $\mathbf{J} = \boldsymbol{\sigma} \cdot \mathbf{E} + \boldsymbol{\alpha} \cdot (-\nabla T)$ [18]. Here σ_{ij} is the conductivity tensor and α_{ij} is the thermoelectric tensor. Setting $\mathbf{J} = 0$ for a finite sample, and solving for \mathbf{E} , we have $\mathbf{E} = -\boldsymbol{\rho} \cdot \boldsymbol{\alpha} \cdot (-\nabla T)$, with $\boldsymbol{\rho} = \boldsymbol{\sigma}^{-1}$ the resistivity tensor. In the geometry with $\mathbf{B} \parallel \hat{\mathbf{z}}$ and $-\nabla T \parallel \hat{\mathbf{x}}$, the components of the E -field, hence the thermopower signal $S_{xx} = -E_x/|\nabla T|$, and the Nernst signal $S_{xy} = E_y/|\nabla T|$, are

$$-S_{xx} = E_x/|\nabla T| = -(\rho_{xx}\alpha_{xx} + \rho_{yx}\alpha_{xy}) \quad (2)$$

$$S_{xy} = E_y/|\nabla T| = \rho_{xx}\alpha_{xy} - \rho_{yx}\alpha_{xx}. \quad (3)$$

We define the sign of the Nernst signal to be that of the y -component of the E -field E_y . More generally, if \mathbf{E}_N is the E -field produced by the Nernst effect, the sign of the Nernst signal is that of the triple product $\mathbf{E}_N \cdot \mathbf{B} \times (-\nabla T)$. This agrees with the old convention based on ‘‘Amperean current’’ [19] and with the one adopted for vortex flow in superconductors [20].

The arguments so far are general which are applicable for all materials. As already mentioned, in Dirac semimetals, AHE [16] and ANE [17] are expected to occur because of the Berry curvature $\boldsymbol{\Omega}_\mathbf{k}$ coming from the Weyl nodes. Indeed, the signatures of the AHE was already manifested in the Hall resistivity ρ_{yx} as weak anomaly at low fields shown in Ref. [12]. The advantage of the Nernst measurements is due to the higher sensitivity [21–23] to the anomalous components. This is because the ther-

moelectric signals are the derivative of the conductivities following the Mott relation [18], viz.,

$$\alpha_{ij} = \mathcal{A} \left[\frac{\partial \sigma_{ij}}{\partial \varepsilon} \right]_{\zeta}, \quad \left(\mathcal{A} = \frac{\pi^2 k_B^2 T}{3e} \right), \quad (4)$$

where k_B is Boltzmann's constant, e is the elemental charge and ζ the chemical potential. Therefore, large anomalous Nernst signals are expected to occur in Dirac semimetal Cd_3As_2 .

Fig. 1 shows the measured Nernst signals at selected temperatures for samples A4, A5, B10, B20 respectively. While both set A and set B samples show sharp anomalous Nernst signals, the anomalous Nernst signals in set A samples dominates the Nernst signals at all temperatures, even up to 200 K. By contrast, for set B samples, conventional semiclassical behavior dominates the signal at high temperatures, and the ANE only becomes prominent at low temperatures. Although strictly speaking the expression Eq. 3 cannot be written as the sum of the conventional and anomalous contribution because Eq. 3 for Nernst signal involves resistivity tensor ρ and thermoelectric tensor α simultaneously, here we phenomenologically express the Nernst signal as following.

$$S_{xy} = S_{xy}^N + S_{xy}^A \quad (5)$$

$$S_{xy}^N = S_0^N \frac{\mu B}{1 + (\mu B)^2} \quad (6)$$

$$S_{xy}^A = \Delta S_{xy}^A \tanh(B/B_0) \quad (7)$$

where μ the mobility, S_0^N the amplitude of the conventional semiclassical contribution S_{xy}^N (for details, see Ref. [24]), ΔS_{xy}^A the amplitude of the anomalous Nernst signal S_{xy}^A , and B_0 the saturation field above which the anomalous Nernst signal reaches its plateau value ΔS_{xy}^A . It turns out that this simple phenomenological expression works well for all samples (except for the minor canting at high fields for A5, B10 and B20). Examples of the fittings is shown for sample A4 in panel B of Fig. 2 which gives good fit at all temperatures. From the fittings, the temperature dependence of the amplitude of the anomalous Nernst signals was extracted, which is plotted in panel A of Fig. 2. Interestingly, while set B samples show small and nearly temperature independent anomalous Nernst amplitude, set A samples show large amplitude of anomalous Nernst signal which increase rapidly below ~ 50 K, suggestive of the close relation between the ANE and the protection mechanism from backscattering that cause ultrahigh mobility as high as $\sim 10^7 \text{ cm}^2 \text{ V}^{-1} \text{ s}^{-1}$ (see Fig. 1 of Ref. [12] and Fig. 2).

Next we briefly discuss the thermopower S_{xx} . The measured signals can be explained by conventional formula for samples A4, B10, B20 (for sample A5, the ultrahigh mobility dramatically distorts the thermopower signals.) The thermopower signals can be described by the conventional semiclassical formula shown below (for

details, see Ref. [24]).

$$S_{xx}(B) = S_0 \frac{1}{1 + (\mu B)^2} + S_{\infty} \frac{(\mu B)^2}{1 + (\mu B)^2} \quad (8)$$

Here, μ the mobility, S_0 and S_{∞} represents the thermopower at zero and infinite magnetic field. For samples A4 and B10, the fittings are shown in panels A, B of Fig. 3, which gives good fits.

Another phenomenon that can be extracted from measuring thermopower and Nernst signals are the beating effect of the quantum oscillations, which was not previously resolved via magnetoresistance (MR) and Hall measurements for the same samples in Ref. [12], another merit of the higher sensitivity of thermopower and Nernst signals [21–23]. Panel C of Fig. 3 plots the oscillation part of Nernst signals of samples A4, A5, B10, B20, which show clear beating effect. Panel D shows the index plots for the average frequency and the envelope frequency of the beating for sample A5. From the slope of the index plot, $S_F^{\text{average}} = 42 \text{ T}$ and $S_F^{\text{envelope}} = 4.5 \text{ T}$ were extracted, which gives the two frequencies $S_1 = 46.5 \text{ T}$ and $S_2 = 37.5 \text{ T}$, showing $\sim 10 \%$ difference from the average value. Similar values were found for other samples A4 ($S_1 = 50.8 \text{ T}$, $S_2 = 44.3 \text{ T}$), B10 ($S_1 = 55.6 \text{ T}$, $S_2 = 46.9 \text{ T}$), B20 ($S_1 = 51 \text{ T}$, $S_2 = 43 \text{ T}$). The beating effect is suggestive of the Dirac nodes splitting into Weyl nodes under magnetic field, causing different Fermi surface areas.

We also investigated the magnetic response of Cd_3As_2 via torque magnetometry for samples A4, A5, B10, B20, whose results are plotted in Fig. 4. As is clear from Fig. 4, every samples except for B10 show “anomalous magnetization” $M_{\tau} \equiv \tau/H$. This is quite surprising considering the fact that Cd_3As_2 consists of no magnetic elements. This raises the question of whether the observed ANE is related to the “anomalous magnetization” or not. For this purpose, we pay attention to the fact that the anomaly of the “anomalous magnetization” is confined well below $\sim 1 \text{ T}$ for all samples at all temperatures and the magnitude of the anomalous component shows little temperature dependence, with the “anomalous magnetization” persisting all the way up to 200 K. By contrast, the anomalous Nernst signals increase rapidly below $\sim 50 \text{ K}$ for set A samples and only show up at low temperatures $\lesssim 15 \text{ K}$ for set B samples. The onset fields of the anomalous Nernst signals also increases up to $\gtrsim 5 \text{ T}$ at 200 K, showing sharp contrast with the “anomalous magnetization” observed. Furthermore, while the ratio of the magnitude for the ANE of samples B20, B10, A4, A5 is $0 : 1 : 3.2 : 7.2$, the ratio of that for the “anomalous magnetization” obtained from SQUID measurements is $0 : 1 : 17.4 : 66.4$, showing large contradictions if they were from the same origin. Therefore, we conclude that the ANE and the “anomalous magnetization” come from different origins.

In conclusion, we have performed detailed study about the thermopower and Nernst effects of Cd_3As_2 for both set A and set B samples. The Nernst signals show clear

ANE suggestive of the existence of Berry curvature Ω_k coming from the Weyl nodes. The magnitude of the anomalous part of Nernst signals can be extracted via the phenomenological expressions Eqs. 5, 6, 7, whose temperature dependence for set A samples show rapid increase below ~ 50 K, where the transport life time τ_{tr} starts to increase, implying close relation in the mech-

anism between the ANE and the remarkable protection mechanism which protects the system from backscattering. High resolution quantum oscillations were extracted from the Nernst signals which give clear beating effect for every samples that was not be able to be resolved via MR and Hall measurements, implying the splitting of Dirac nodes into Weyl nodes.

-
- [1] Hosur, P. & Qi, X. Recent developments in transport phenomena in Weyl semimetals. *Comptes Rendus Physique* **14**, 857 – 870 (2013).
 - [2] Murakami, S. Phase transition between the quantum spin Hall and insulator phases in 3D: emergence of a topological gapless phase. *New Journal of Physics* **9**, 356 (2007).
 - [3] Murakami, S. & Kuga, S.-i. Universal phase diagrams for the quantum spin Hall systems. *Phys. Rev. B* **78**, 165313 (2008).
 - [4] Xu, S.-Y. *et al.* Observation of Fermi arc surface states in a topological metal. *Science* **347**, 294–298 (2015).
 - [5] Wang, Z., Weng, H., Wu, Q., Dai, X. & Fang, Z. Three-dimensional Dirac semimetal and quantum transport in Cd_3As_2 . *Phys. Rev. B* **88**, 125427 (2013).
 - [6] Wang, Z. *et al.* Dirac semimetal and topological phase transitions in $A_3\text{Bi}$ ($A = \text{Na}, \text{K}, \text{Rb}$). *Phys. Rev. B* **85**, 195320 (2012).
 - [7] Nielsen, H. & Ninomiya, M. The adler-bell-jackiw anomaly and weyl fermions in a crystal. *Physics Letters B* **130**, 389 – 396 (1983).
 - [8] Son, D. T. & Spivak, B. Z. Chiral anomaly and classical negative magnetoresistance of Weyl metals. *Phys. Rev. B* **88**, 104412 (2013).
 - [9] Xiong, J. *et al.* Evidence for the chiral anomaly in the Dirac semimetal Na_3Bi . *Science* **350**, 413–416 (2015).
 - [10] Hirschberger, M. *et al.* The chiral anomaly and thermopower of Weyl fermions in the half-Heusler GdPtBi . *ArXiv e-prints* (2016). 1602.07219.
 - [11] Kim, H.-J. *et al.* Dirac versus Weyl Fermions in Topological Insulators: Adler-Bell-Jackiw Anomaly in Transport Phenomena. *Phys. Rev. Lett.* **111**, 246603 (2013).
 - [12] Liang, T. *et al.* Ultrahigh mobility and giant magnetoresistance in the Dirac semimetal Cd_3As_2 . *Nat Mater* **14**, 280–284 (2015).
 - [13] Zhang, C. *et al.* Detection of chiral anomaly and valley transport in Dirac semimetals. *ArXiv e-prints* (2015). 1504.07698.
 - [14] Li, Q. *et al.* Observation of the chiral magnetic effect in ZrTe_5 . *ArXiv e-prints* (2014). 1412.6543.
 - [15] Zhang, C. *et al.* Observation of the Adler-Bell-Jackiw chiral anomaly in a Weyl semimetal. *ArXiv e-prints* (2015). 1503.02630.
 - [16] Xiao, D., Chang, M.-C. & Niu, Q. Berry phase effects on electronic properties. *Rev. Mod. Phys.* **82**, 1959–2007 (2010).
 - [17] Sharma, G., Goswami, P. & Tewari, S. Nernst and magneto-thermal conductivity in a lattice model of Weyl fermions. *ArXiv e-prints* (2015). 1507.05606.
 - [18] Ziman, J. M. *Electrons and Phonons* (Oxford Clarendon Press, Oxford, 1960)p 500. .
 - [19] Bridgman, P. W. The Connections between the Four Transverse Galvanomagnetic and Thermomagnetic Phenomena. *Phys. Rev.* **24**, 644–651 (1924).
 - [20] Wang, Y., Li, L. & Ong, N. P. Nernst effect in high- T_c superconductors. *Phys. Rev. B* **73**, 024510 (2006).
 - [21] Behnia, K., Méasson, M.-A. & Kopelevich, Y. Oscillating Nernst-Ettingshausen Effect in Bismuth across the Quantum Limit. *Phys. Rev. Lett.* **98**, 166602 (2007).
 - [22] Zhu, Z., Fauqué, B., Fuseya, Y. & Behnia, K. Angle-resolved Landau spectrum of electrons and holes in bismuth. *Phys. Rev. B* **84**, 115137 (2011).
 - [23] Zhu, Z. *et al.* Quantum Oscillations, Thermoelectric Coefficients, and the Fermi Surface of Semimetallic WTe_2 . *Phys. Rev. Lett.* **114**, 176601 (2015).
 - [24] Liang, T. *et al.* Evidence for massive bulk Dirac fermions in $\text{Pb}_{1-x}\text{Sn}_x\text{Se}$ from Nernst and thermopower experiments. *Nat Commun* **4**, – (2013).

*These authors contributed equally to this work.

Acknowledgements T.L. acknowledges a scholarship from Japan Student Services Organization. N.P.O. acknowledges the support of the U.S. National Science Foundation (Grant DMR 1420541) and the Gordon and Betty Moore Foundations EPiQS Initiative through Grant GBMF4539.

Author Information The authors declare no competing financial interests. Correspondence and requests for materials should be addressed to T.L. (tliang@princeton.edu) and N.P.O. (npo@princeton.edu).

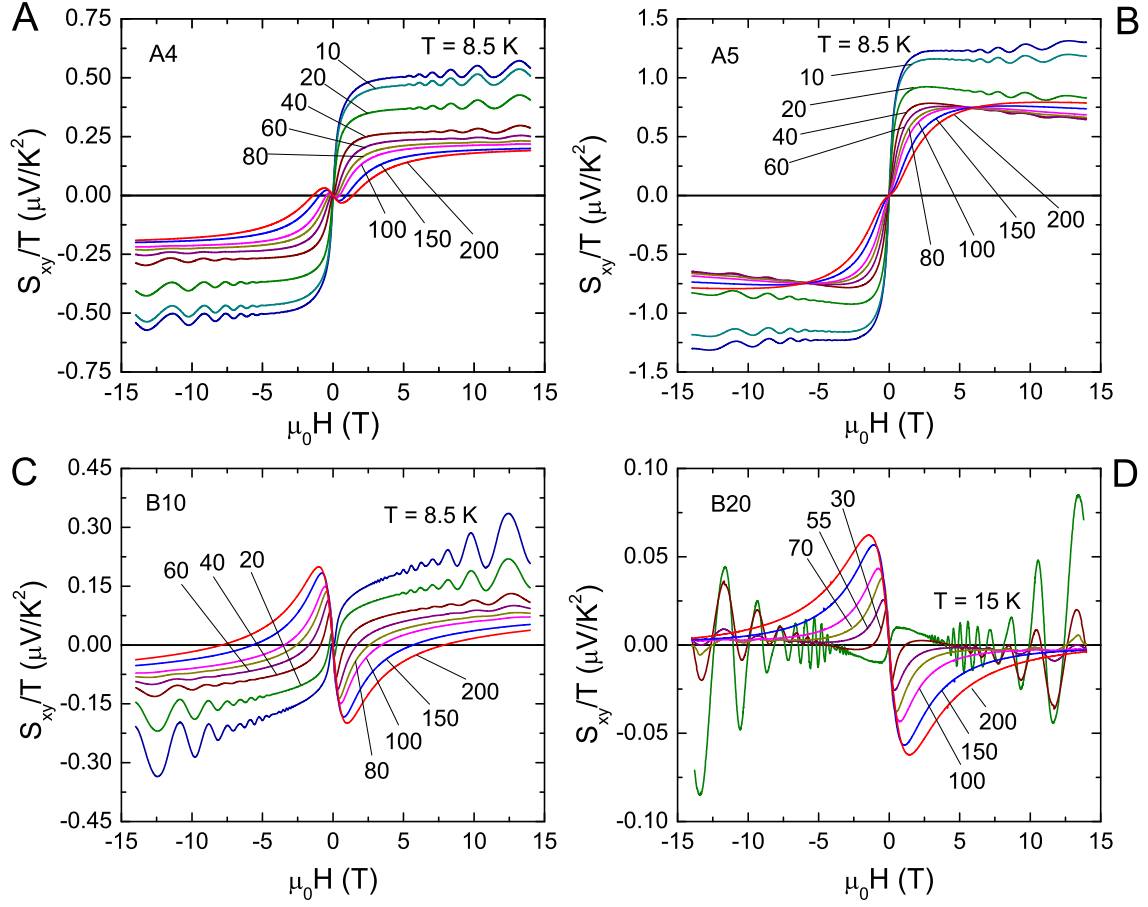


FIG. 1: (color online). Nernst effect at selected temperatures for samples A4 (Panel A), A5 (Panel B), B10 (Panel C), and B20 (Panel D), showing ANE for every sample. In the set A samples A4 and A5, giant Nernst signals develop even from 200 K. By contrast, the conventional Drude-like signal dominates in set B samples B10 and B20 except for the low temperature regimes, where the ANE grows.

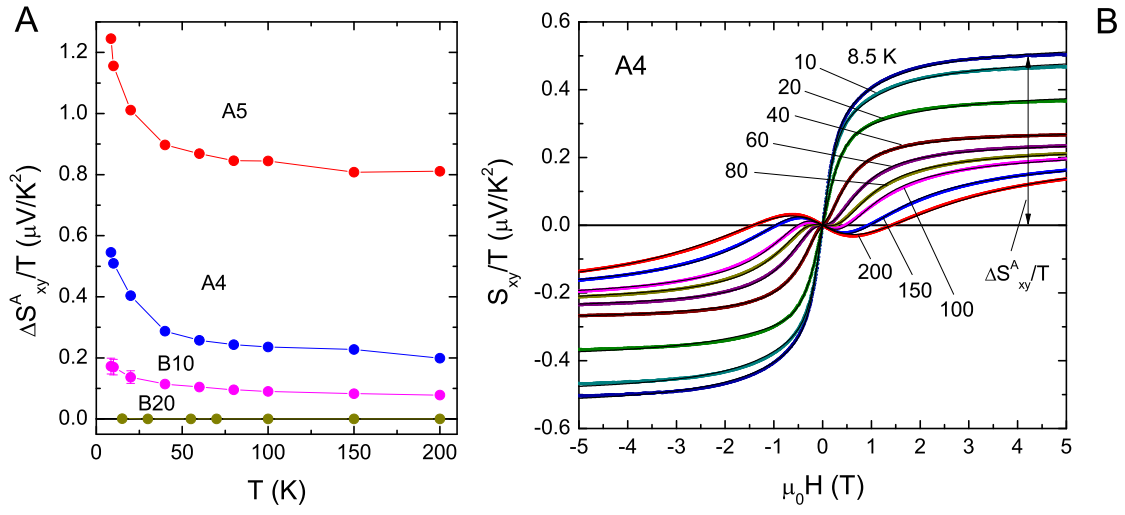


FIG. 2: (color online). Panel A: Temperature dependence of the amplitude of anomalous Nernst signal $\Delta S^A_{xy}/T$. In the set A samples A4 and A5, the magnitude of anomalous Nernst signals develops rapidly below 50 K, suggestive of the correlation with the protection mechanism from the backscattering. Panel B: Fittings to the observed Nernst effect for sample A4. The observed Nernst effect was fit to the phenomenological expression (Eqs. 5, 6, 7 in the main text) $S_{xy} = S_0^N \mu B / (1 + (\mu B)^2) + \Delta S^A_{xy} \tanh(B/B_0)$, where S_0^N and ΔS^A_{xy} represent the amplitude of normal and anomalous part of Nernst signals respectively. The fitted lines are shown in black, showing good match with the data.

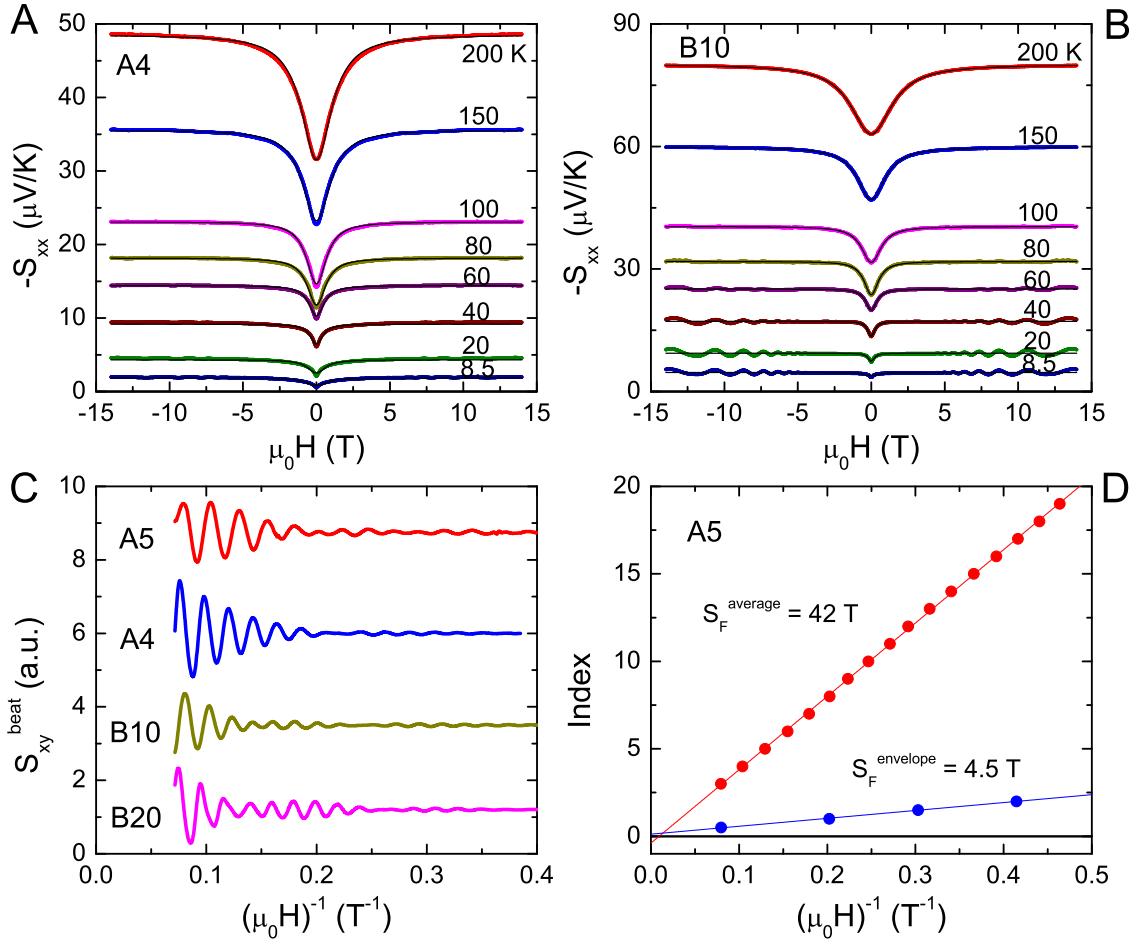


FIG. 3: (color online). Panels A and B show the Seebeck signals of sample A4 (left panel) and B10 (right panel) at selected temperatures. The Seebeck signals can be fit using semiclassical expression of Eq. 8 in the main text. Panel C shows the oscillation part of the Nernst signals for each sample. Clear beatings were observed for every sample, suggestive of the splitting of Dirac nodes into Weyl nodes. Panel D shows the index plot of sample A5 for average frequency and the envelope frequency, yielding the two Fermi surface areas to be $S_1 = 46.5 \text{ T}$ and $S_2 = 37.5 \text{ T}$ respectively.

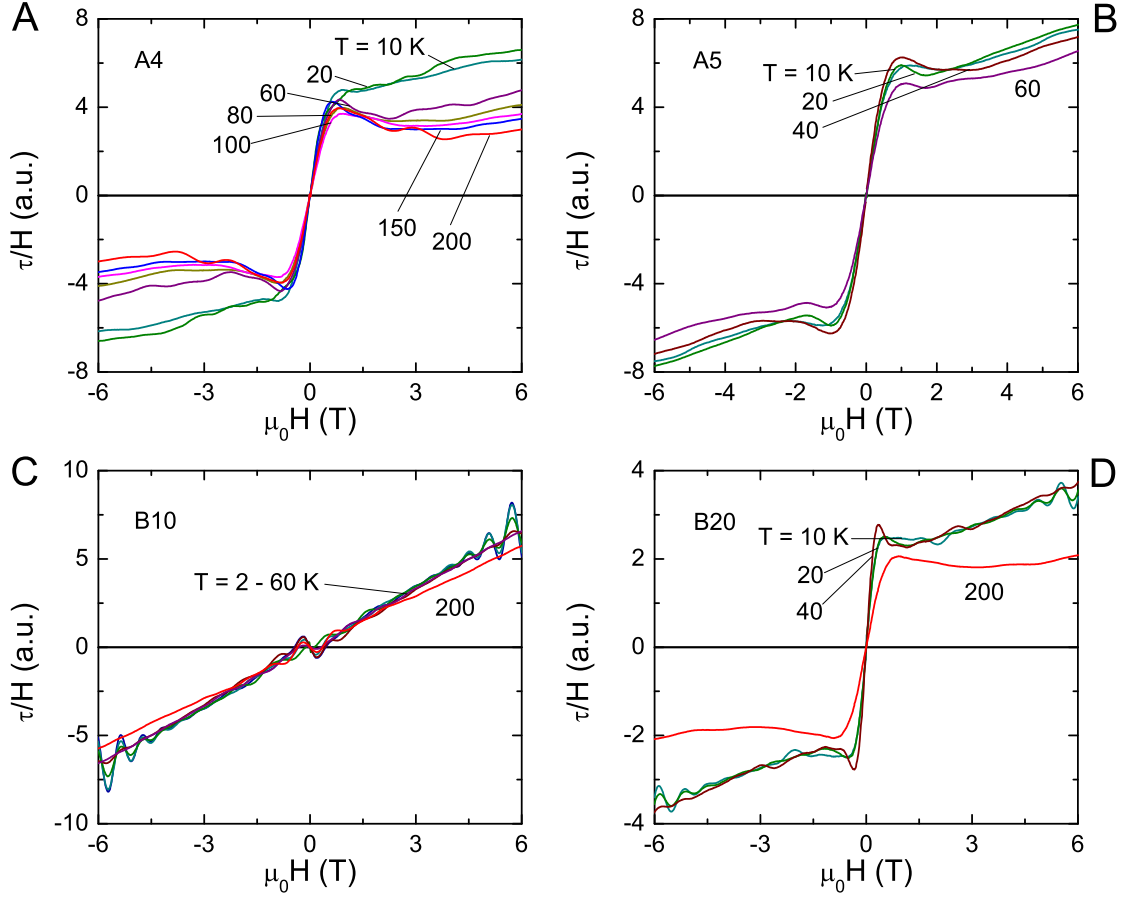


FIG. 4: (color online). “Anomalous magnetization” $M_\tau \equiv \tau/H$ at selected temperatures obtained from torque magnetometry for samples A4, A5, B10, B20. The anomalous part is confined well below 1 T for all samples at all temperatures with the magnitude almost independent of the temperature, having sharp contrast with the anomalous Nernst signals shown in Fig. 1, suggestive of their different origins.